Almeida, Humberto; Jayaprakash, Siddharth; Kolari, Kari; Kuva, Jukka; Kukko, Kirsi; Partanen, Jouni

The role of printing parameters on the short beam strength of 3D-printed continuous carbon fibre reinforced epoxy-PETG composites

Published in:
Composite Structures

DOI:
10.1016/j.compstruct.2024.118034

Published: 15/03/2024

Document Version
Publisher's PDF, also known as Version of record

Please cite the original version:
Almeida, H., Jayaprakash, S., Kolari, K., Kuva, J., Kukko, K., & Partanen, J. (2024). The role of printing parameters on the short beam strength of 3D-printed continuous carbon fibre reinforced epoxy-PETG composites. *Composite Structures*, *337*, Article 118034. https://doi.org/10.1016/j.compstruct.2024.118034

Composite Structures 337 (2024) 118034

Contents lists available at ScienceDirect

Composite Structures

journal homepage: www.elsevier.com/locate/compstruct

The role of printing parameters on the short beam strength of 3D-printed continuous carbon fibre reinforced epoxy-PETG composites

José Humberto S. Almeida Jr. [a,b,*], Siddharth Jayaprakash [c], Kari Kolari [d], Jukka Kuva [e], Kirsi Kukko [c], Jouni Partanen [c]

[a] School of Mechanical and Aerospace Engineering, Queen's University Belfast, Belfast, UK
[b] Department of Mechanical Engineering, LUT University, Lappeenranta, Finland
[c] Department of Mechanical Engineering, Aalto University, Espoo, Finland
[d] VTT Technical Research Centre of Finland, Espoo, Finland
[e] Geological Survey of Finland GTK, Espoo, Finland

ARTICLE INFO

Dataset link: https://doi.org/10.23729/ebe7a8e4-1a16-4dac-8867-015b07cd3971

Keywords:
3D printing parameters
Additive manufacturing
Interlaminar strength
Statistical analysis
Failure analysis
Microstructure

ABSTRACT

It is well known that printing parameters strongly affect the mechanical performance of 3D printed parts. This work explores the role of i) extruder temperature, ii) print speed, and iii) layer height on the interlaminar strength of 3D-printed continuous fibre-reinforced composites. The carbon fibre-reinforced thermoset filament is printed concomitantly with polyethylene terephthalate glycol (PETG) thermoplastic filament in a single nozzle, characterising a continuous fibre co-extrusion (CFC) process. There is a significant variation in the short beam strength for composites printed with different parameters. The load–displacement curves have a similar pattern, with clear load peaks followed by a plastic zone. Optical micrographs and computed tomography (CT) scans reveal that the microstructure is dependent on the printing parameters. Image analysis elucidates the various mechanisms of void formation. Following the application of a three-way ANOVA and statistical tests to quantify the effects and interactions among variables, the analysis concludes that the extruder temperature has the highest influence, followed by print speed and layer height. When considering all possible interactions between the factors, the interaction between print speed and layer height is the most impactful.

1. Introduction

Compared to conventional manufacturing processes for fibre-reinforced composites, 3D printing offers more design freedom to manufacture lightweight complex parts with outstanding mechanical properties [1–3]. Key advantages of composite 3D printing include design flexibility, waste reduction, customisation of properties, prototyping and rapid interaction, and multi-functionality [4–6]. Moreover, by combining continuous fibre filaments [7] with polymeric filaments, it becomes possible to produce unidirectional fibre-reinforced composites that leverage the inherent anisotropy of carbon fibres. This enables the 3D printing of composites with elevated stiffness- and strength-to-weight ratios [8–10]. The very first 3D printer capable of printing composites with continuous fibre was the Mark One from MarkForged, released back in 2014, which employs the principles of the fused filament fabrication (FFF) technique. The first related scientific work was published in 2016, where Tian et al. [11] developed 3D-printed continuous carbon fibre-reinforced polylactic acid (PLA) composites. Therefore, it is natural that the role of processing parameters on the mechanical properties of 3D printed composites is not fully understood yet. Penumakala et al. [12], Kabir et al. [13], Safari et al. [14] and Zhang et al. [15] conducted reviews on the effects of pre- and post-processing parameters of 3D printed continuous carbon fibre (CCF) reinforced polymer composites on their mechanical properties. A key conclusion from these reviews is that the influence of printing parameters on the mechanical properties of CCF composites is still unknown and should be further investigated.

It is well known that any additive manufacturing (AM) process is strongly dependent on the printing parameters [14]. Unsuitable parameters can significantly reduce the mechanical, thermal, and physical properties of the part [16]. In an attempt to summarise the printing effects for 3D printed continuous fibre composites, Kabir et al. [13] conducted a review of 3D printed CCF composites and concluded that the printing and process parameters are still exploratory and no conclusions about their roles could be drawn. Dou et al. [17] analysed CCF-PLA composites and found out that when the printing layer height

* Corresponding author at: School of Mechanical and Aerospace Engineering, Queen's University Belfast, Belfast, UK.
E-mail addresses: humberto.almeida@qub.ac.uk (J.H.S. Almeida Jr.), siddharth.jayaprakash@aalto.fi (S. Jayaprakash), kari.kolari@vtt.fi (K. Kolari), jukka.kuva@gtk.fi (J. Kuva), kirsi.kukko@aalto.fi (K. Kukko), jouni.partanen@aalto.fi (J. Partanen).

https://doi.org/10.1016/j.compstruct.2024.118034
Received 8 August 2023; Received in revised form 21 November 2023; Accepted 12 March 2024
Available online 15 March 2024

increases from 0.2 to 0.4 mm and the extrusion width increases from 0.86 to 1.5 mm, tensile properties decrease. When the printing temperature increases from 190 to 230 °C and the printing speed increases from 50 to 400 mm/min, the tensile properties gradually decrease. Rimašauskas et al. [18] studied the influence of the height and width of the line on the formation of voids and the tensile strength of CCF-PLA composites. They found that the lower the layer height and line width, the higher the tensile strength. Dong et al. [19] studied the effects of fibre content and cell length on 3D cellular structures made of Kevlar fibre reinforced PLA composites in tension. They reported an increase in tensile properties with higher fibre content and a negative effect on shape-memory performance. Liu et al. [2] 3D printed and analysed CCF-PETG composites in 3-point bending tests with several extruder temperatures, print speeds, hatch spacing and layer heights. They found that the nozzle temperature between 230 °C and 250 °C, print speed below 7.5 mm/s, and the short hatch spacing favour the bending strength and modulus. The layer height effect was not conclusive. They concluded that more comprehensive mechanical testing should be conducted to understand printing parameters and correlate them with mechanical properties and printing defects. Maqsood and Rimašauskas [20] analysed the effects of printing parameters and cooling on the mechanical properties of CCF-reinforced PLA composites, concluding that using extrusion temperature of 230 °C, extrusion width of 1.2 mm, and extrusion multiplier of 0.7 provided the highest tensile and bending strengths. Jia et al. [21] explored CCF-reinforced PLA composites and concluded that layer height of 0.05 mm, print speed of 250 mm/min and extruder temperature of 210 °C provided the highest tensile strength. While the impact of printing parameters on the mechanical performance of continuous carbon fibre reinforced polymers (CCFRPs) has been investigated, and research has explored the interlaminar properties of 3D printed composites [22,23], there remain unanswered questions regarding the influence of printing parameters on the interlaminar strength of such 3D printed composites.

To address this gap, this paper aims to reveal the impact of 3D printing parameters on the interlaminar behaviour of CCF-reinforced PETG composites. The parameters varied are (i) extruder temperature, (ii) print speed, and (iii) layer height. Their effects are observed in the short beam shear test, an established testing method to evaluate the interlaminar performance of continuous-fibre composites. To support the experimental findings, a robust statistical treatment is performed using three-way ANOVA, and several statistical tests are applied to the dataset to quantify the effects and interactions between factors. Furthermore, stereo micrographs, optical micrographs, and X-ray Computed Tomography (CT) scans are carried out on pristine and fractured samples to characterise both the microstructure and failure mechanisms of the printed composites.

2. Experimental details

2.1. Design of experiments

In this study, the extruder temperature, print speed, and layer height are varied, and their effects are observed on the short beam strength of the parts. This well-established test is very effective in quantifying the interlaminar strength of composite parts. The design of experiments (DoE) is performed such that there are three independent factors/variables: (i) extruder temperature, (ii) print speed, and (iii) layer height. The dependent factor/variable is the short beam strength (SBS). The complete DoE is described in Table 1. As per Table 1, the nomenclature adopted in this study follows the 3D printing parameters (i.e., the independent factors, in the context of the statistical analysis). For instance, a sample printed with a *layer height of* ***0.24 mm***, *extruder temperature of* **200 °*C***, and *print speed coefficient of* ***0.4*** is coded as ***0.24_200_0.4***. The same logic is used for all families of samples described in Table 1 and throughout the work.

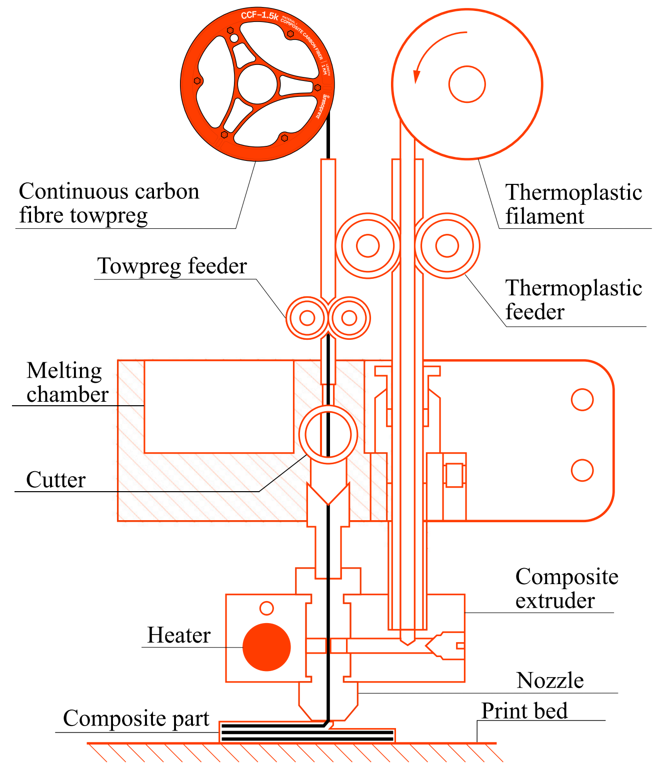

Fig. 1. Schematic representation of the composite fibre co-extrusion (CFC) process. *Source:* Adapted from [24].

It is important to note that in the 3D printer utilised in this study, the printing speed is regulated through a coefficient linked to fibre print speeds. Consequently, the speeds detailed in Table 1 encompass the print coefficient, constant print speed during the contour (zigzag area, as illustrated in Fig. 2), and the speed along the deposition of straight composite lines. The contour print speed encompasses both extrusion and non-extrusion movements during direction changes, as well as the initial speed of the straight composite lines (y-axis in Fig. 2). When the print speed coefficient is changed, the contour print speed remains constant (as predetermined by the developer), while the speed of deposition of straight composite lines along the y-axis changes accordingly.

2.2. Additive manufacturing

The in-place 3D printing method is a variation of the FFF technique [25], in which the fibre yarns are embedded in a molten thermoplastic polymer during the extrusion process. The yarn is composed of continuous carbon fibre tows pre-impregnated (towpreg) with a epoxy thermoset polymer. This filament can then be considered to be a two-matrix system, which brings together the advantages of thermoset and thermoplastic polymers intermingled with continuous carbon fibres. In a nutshell, the epoxy thermoset matrix provides bonding between fibre filaments in the tow, whereas the thermoplastic polymer boosts both interlaminar and impact strength. During the printing process, the towpreg and polymer filaments (polyethylene terephthalate glycol - PETG - is used here) are fed from independent tubes into a melting chamber, heated and mixed in a single nozzle and are then concomitantly deposited by co-extrusion. The FFF technique employed here is a modified version known as the composite fibre coextrusion (CFC) process. The CFC process is illustrated in Fig. 1 for a better understanding.

The two spools represented in Fig. 1 are made of:

Table 1
Design of experiments (DoE) and nomenclature for the composites manufactured with different printing parameters.

Nomenclature	Layer height (mm)	Extruder temperature (°C)	Print speed Coefficient (–)	Contour (mm/s)	Variable (mm/s)
0.24_200_0.4	0.24	200	0.4	2	4
0.24_200_0.5	0.24	200	0.5		5
0.24_200_0.6	0.24	200	0.6		6
0.24_210_0.4	0.24	210	0.4		4
0.24_210_0.5	0.24	210	0.5		5
0.24_210_0.6	0.24	210	0.6		6
0.24_220_0.4	0.24	220	0.4		4
0.24_220_0.5	0.24	220	0.5		5
0.24_220_0.6	0.24	220	0.6		6
0.34_200_0.4	0.34	200	0.4		4
0.34_200_0.5	0.34	200	0.5		5
0.34_200_0.6	0.34	200	0.6		6
0.34_210_0.4	0.34	210	0.4		4
0.34_210_0.5	0.34	210	0.5		5
0.34_210_0.6	0.34	210	0.6		6
0.34_220_0.4	0.34	220	0.4		4
0.34_220_0.5	0.34	220	0.5		5
0.34_220_0.6	0.34	220	0.6		6

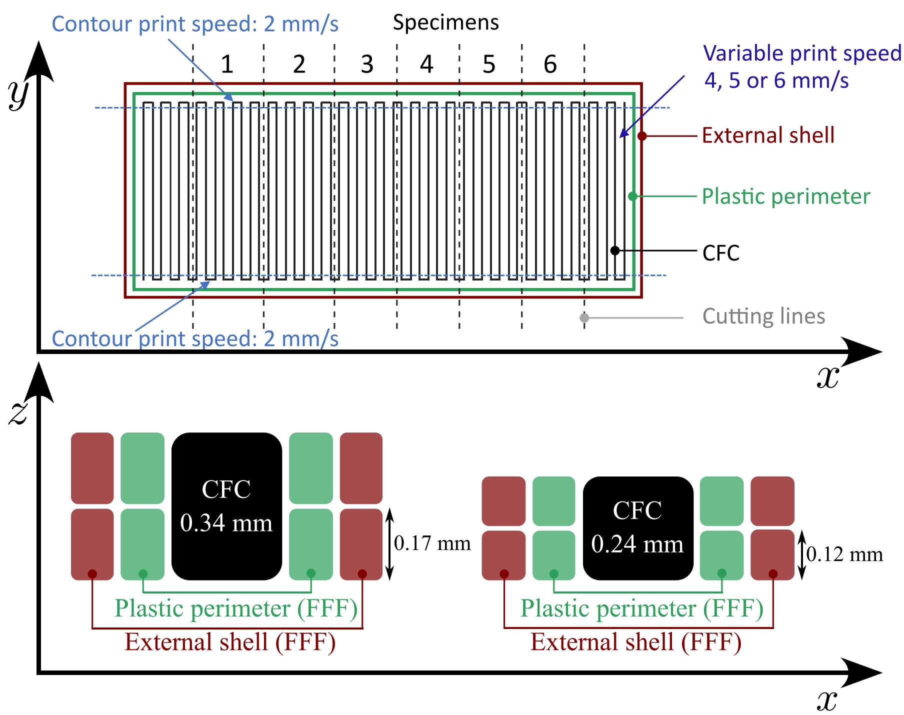

Fig. 2. Schematic general representation of different views (x–y plane at the top and $x-z$ plane at the bottom) of the microstructure of a single layer for the printed composites with different macrolayer thicknesses.

- Towpreg - CCF yarn pre-impregnated with epoxy from Anisoprint (1.5k carbon fibres), with a filament diameter of 0.35 mm at a fibre volume fraction of 60%; and
- Transparent PETG with filament diameter of 1.75 mm and density of 1.3 g/cm^3

The desktop 3D printer used here is from Anisoprint, model Composer A4, which has a build volume of 297 × 210 × 140 mm. The printer utilises a dual-extrusion system, i.e., there are two print nozzles – a CFC printhead and a separate FFF printhead. The FFF nozzle extrudes the thermoplastic filament (PETG in this case) to create the external shell, plastic perimeters, and top/bottom solid layers, in places where a composite layer contacts the external environment. It also helps to provide stability to the surfaces of the part. The FFF nozzle has a diameter of 0.4 mm, and it extrudes the thermoplastic filament with a cold starting diameter of 1.75 mm.

The design of the parts, sized 70 × 18 × 3.5 mm, is sliced using Aura slicing software. In total, 18 print profiles are created by varying the three independent printing parameters selected as part of the DoE (see Table 1). The external shell and plastic perimeters are printed at a rate of 30 mm/s and 50 mm/s, respectively. Extrusion width, the width of the extruded composite material (towpreg + PETG), is set to 0.65 mm. The parts are printed on a preheated print bed at 60 °C and inside a chamber at 25 °C.

All the composite part profiles are 3D printed with solid reinforced infill. In other words, the entire inner space of the parts is made with 100% density via CFC. The CFC infill is deposited at an angle (guide direction) of 90° to the x-axis. Fig. 2 illustrates the layer structure of printed parts with layer heights of 0.34 mm and 0.24 mm, respectively. Here, the layer height refers to the macrolayer height, that is, the height of an individual layer within the printed part. Each macrolayer contains microlayers that are made of one or more print entities with the same

Table 2
Printing details for the composites manufactured with different printing parameters.

Nomenclature	Print time (min)	Macrolayers	Polymer used in CFC/FFF extruders (m)	Towpreg used (m)
0.24_200_0.4	187	10	0.5/0.4	18.1
0.24_200_0.5	179	10	0.5/0.4	18.1
0.24_200_0.6	173	10	0.5/0.4	18.1
0.24_210_0.4	187	10	0.5/0.4	18.1
0.24_210_0.5	179	10	0.5/0.4	18.1
0.24_210_0.6	173	10	0.5/0.4	18.1
0.24_220_0.4	187	10	0.5/0.4	18.1
0.24_220_0.5	179	10	0.5/0.4	18.1
0.24_220_0.6	173	10	0.5/0.4	18.1
0.34_200_0.4	117	6	0.6/0.5	10.9
0.34_200_0.5	112	6	0.6/0.5	10.9
0.34_200_0.6	109	6	0.6/0.5	10.9
0.34_210_0.4	117	6	0.6/0.5	10.9
0.34_210_0.5	112	6	0.6/0.5	10.9
0.34_210_0.6	109	6	0.6/0.5	10.9
0.34_220_0.4	117	6	0.6/0.5	10.9
0.34_220_0.5	112	6	0.6/0.5	10.9
0.34_220_0.6	109	6	0.6/0.5	10.9

height. In this setup, there are two microlayers within each macrolayer. The first microlayer includes an external shell and a plastic perimeter, while the second includes the CFC infill, the external shell, and the plastic perimeter. Fig. 2 schematically shows the CFC infill layer height, which is always equal to the macrolayer height.

Table 2 shows the total print time, the number of reinforced layers (macrolayers), the total amount of towpreg used, and the total polymer filament used by the FFF and CFC print heads. For further information on the slicing settings and printing parameters, g-codes for all 18 print profiles and the Anisoprint Aura project file are appended as supplementary material for reproduction purposes. After 3D printing, the parts are wet-cut using a diamond saw (cutting lines are shown in Fig. 2), and the samples are then polished with sandpaper to remove burs and jagged edges. At least ten samples of each family are prepared.

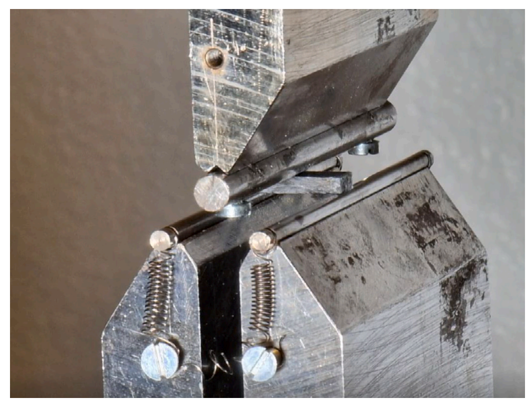

Fig. 3. The short beam shear testing rig.

2.3. Testing

The tests are designed and performed according to the ASTM D2344/D2344M-22 standard. All composite samples are tested for short beam testing in an MTS universal testing machine equipped with a load cell of 30 kN (Fig. 3). The span-to-thickness ratio of the samples is 4:1, while the length l and the width w are 6× and 2× the thickness t, respectively. The loading nose and supports have diameters of 6 mm and 3 mm, respectively. The load is controlled by displacement with a load rate of 1 mm/min. Five validated tests for each family of sample are considered in both mechanical and statistical analyses. The SBS is defined as SBS = $(3 \times L_{max})/(4 \times w \times t)$, where L_{max} is the maximum load and w is the width of the sample.

2.4. Statistical analysis

Given a large amount of data and the complexity of correlating them, a 3-way (also known as three-factor) analysis of variance (ANOVA) is employed to quantify the effects that the three distinct factors have on the dependent outcome [26]. The independent factors (variables) are (i) extruder temperature, (ii) print speed, and (iii) layer height. The dependent factor (variable) is the SBS. These three independent factors may each have a distinguishable effect on the dependent factor. They may also interact with each other. Three-way ANOVA allows for quantifying the effects of each and whether the factors interact. Besides the exploration of the 3-way ANOVA features, the following statistical tests are applied to quantify statistical significance, main effects, and interactions between factors:

- Levene test [27]: utilises an F-test to assess the null hypothesis, which posits equal variance across groups. A p-value below 0.05 signifies a deviation from this assumption. In the event of a violation, opting for the non-parametric equivalent analysis is likely more suitable;
- Shapiro–Wilk test [28]: it is a hypothesis test used to assess the normal distribution of a dataset. The null hypothesis assumes that the data set follows a normal distribution. A high p-value suggests normal distribution, while a low p-value suggests deviation from normal distribution; and
- Eta squared [29]: Eta squared serves as an effect size metric for ANOVA models. It provides a standardised estimation of effect size, enabling comparisons across outcome variables measured in different units.

All statistical analyses and tests are performed in R environment, using RStudio integrated development environment for R language. All the equations and fundamentals used in the ANOVA and statistical tests used in this work can be found in the R documentation. Besides, all chunks of codes developed to generate the results are presented in Appendix A. In addition, the entire dataset is uploaded as a Supplementary Material.

Three-way ANOVA helps to assess the following primary elements:

- The primary impact of each of the three separate variables;
- The interaction effect between every combination of two factors (A × B, A × C, B × C); and
- The mutual influence of all three factors combined (A × B × C).

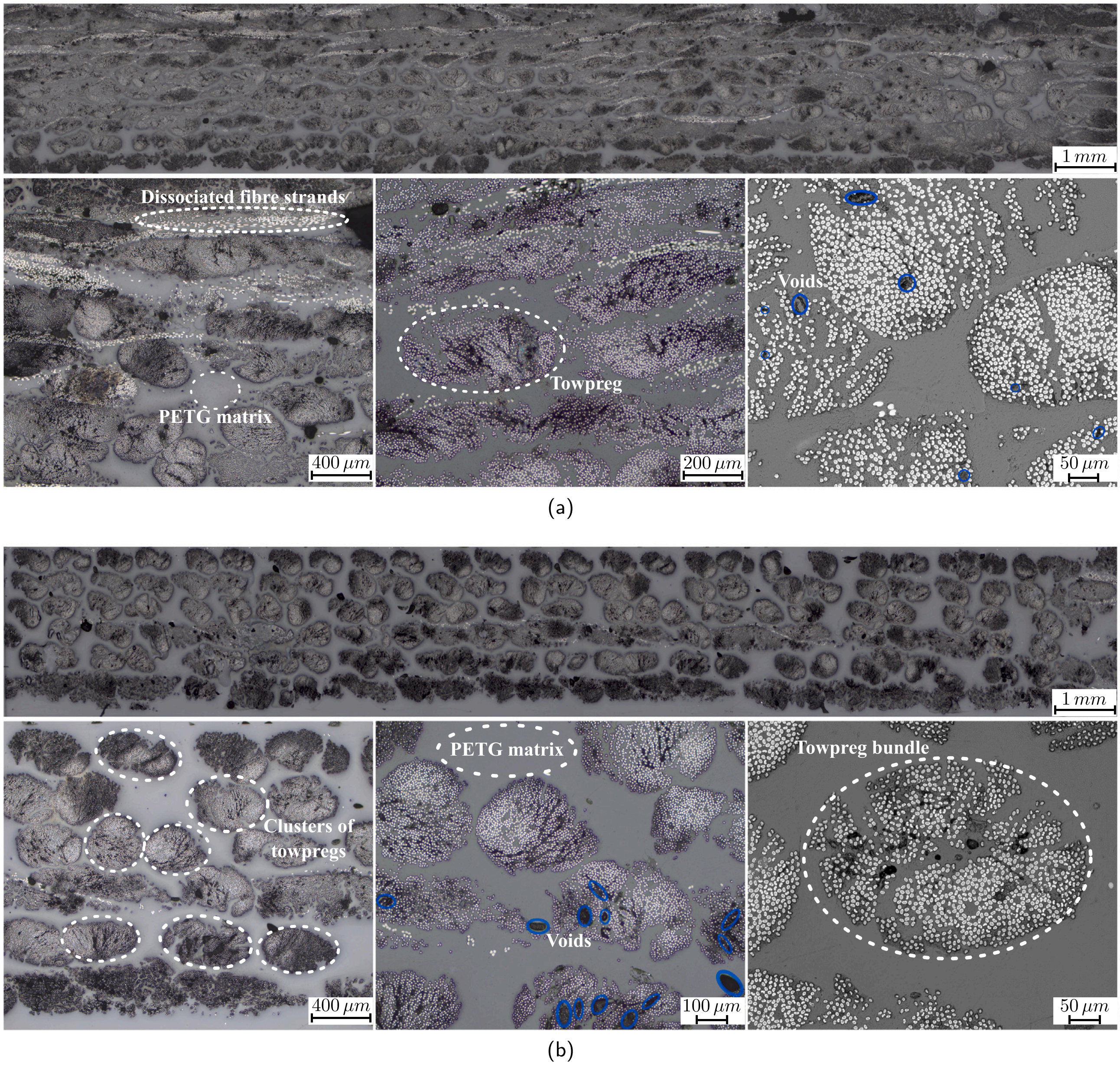

Fig. 4. Optical micrographs of samples (a) 0.24_200_0.6 and (b) 0.34_220_0.5.

The main equation to conduct the 3-way ANOVA can be summarised as:

$$Y = \mu + \alpha_i + \beta_j + \gamma_k + (\alpha\beta)_{ij} + (\alpha\gamma)_{ik} + (\beta\gamma)_{jk} + (\alpha\beta\gamma)_{ijk} + \varepsilon_{ijk} \quad (1)$$

where Y is the dependent variable, μ is the overall mean, α, β, and γ are the main effects of each factor, $\alpha\beta$, $\alpha\gamma$ and $\beta\gamma$ represent the pair-wise interaction, $\alpha\beta\gamma$ is the 3-way interaction, and ϵ stands for the residual or error.

2.5. Image analysis

2.5.1. Microstructure characterisation

To describe the microstructure of the samples, two methods are utilised: optical micrographs and X-ray CT scans. Two sample families are selected for microstructure characterisation: 0.24_200_0.6 and 0.34_220_0.5. The specifics of each analysis are outlined below:

- Optical micrographs: to better understand the microstructure of the 3D-printed composites, samples are cut and embedded in transparent epoxy resin and images are taken using a ZEISS Axio Observer optical microscope.
- CT scanning: to investigate the 3D microstructure of the composite samples, they are scanned using a GE Phoenix v|tome|x s. The samples are scanned in a single scan with an accelerating voltage of 100 kV and a tube current of 120 μA for a total power of 12 W. In a 360° rotation, 2,700 radiographs are taken. At every step, the detector waits for a single exposure time and then takes an average of over three exposures. With a single exposure time of 500 ms, the total scan time is 90 min. The obtained resolution is of 12.2 μm. Ring artefacts are reduced in the reconstruction of the images, but no beam hardening correction is used. Image visualisation and void content are performed using ThermoFisher PerGeos 2020.2 and Marker-Based Watershed.

2.5.2. Failure analysis

Photographs of fractured samples are taken using an Olympus EM1-Mark II digital camera with an Olympus M. Zuiko Digital ED 60 mm

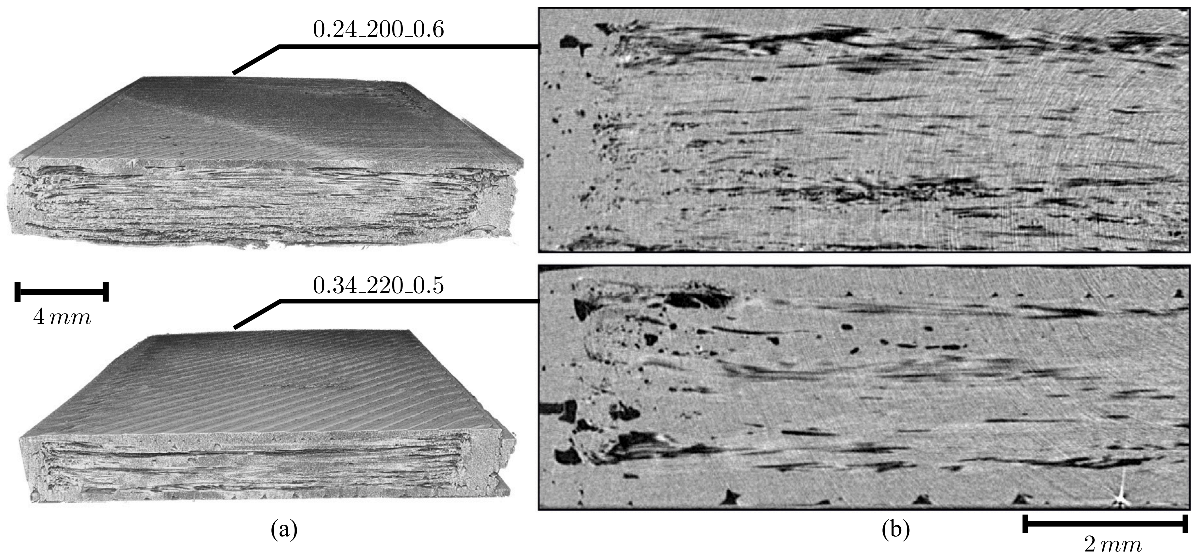

Fig. 5. Microstructure characterisation of as-printed samples through CT scans: (a) 3D renders and (b) 2D cross-sections images of samples 0.24_200_0.6 and 0.34_220_0.5.

F2.8 macro lens. The camera is attached to a Kaiser shooting table with adjustable lights. Failure modes are examined using a ZEISS Axio Zoom V16 stereo microscope. CT scans of selected samples are also taken (using the same methodology and equipment for the microstructure characterisation) to further analyse their failure behaviour.

3. Results and discussion

While the dataset and the extent of analyses are deemed comprehensive and adequately robust for the current research, it is essential to acknowledge limitations of this study. They encompass: (i) the scope of assessed printing parameters (such as higher speeds or temperatures); (ii) exploration of alternative loading cases; and (iii) evaluation of other materials. The limitations identified are not incorporated into the current study as they fall outside the scope of our research. However, they will be taken into account in future investigations.

3.1. Microstructure characterisation

Optical micrographs and X-ray CT scans are taken for samples 0.24_200_0.6 and 0.34_220_0.5 to show the differences in their microstructures when printed with completely different printing parameters. In addition, as can be further seen in Section 3.2, it is worth mentioning that the samples 0.24_200_0.6 and 0.34_220_0.5 have the lowest and highest SBS, respectively.

The optical micrographs shown in Fig. 4 reveal the 2D microstructure for samples 0.24_200_0.6 (Fig. 4(a)) and 0.34_220_0.5 (Fig. 4(b)). The sample 0.24_200_0.6 is 3D printed with a layer height of 0.24 mm and it has more CCF towpreg in the microstructure than the sample 0.34_220_0.5. This association between layer height and the amount of towpreg present is illustrated in Fig. 2 and Table 2. Looking at Figs. 4 and 5 (CT scans), it is observed that the distribution of PETG matrix around the towpreg is more homogeneous in the 0.34_220_0.5 sample - implying a more uniform impregnation of towpreg (CCF-epoxy-bundles) and also better adhesion between macrolayers, which reduces the likelihood of delamination.

The microstructure of the sample 0.24_200_0.6 exhibits a notably dense packing of towpregs toward its upper region, with indistinct separation between macrolayers and the composite strands laterally arranged within each layer. This lack of separation is attributed to heightened contact pressure between the composite (towpreg-PETG) strand and the CFC nozzle, particularly evident in the upper layers. In a related study, Wang et al. [30] explored the relation between the impregnation process and contact pressure in CCF-reinforced PLA 3D printed composites. Their findings indicated that the majority of impregnation occurred during the nozzle-squeezing phase during filament deposition. Interestingly, for a single extruded composite strand, impregnation improved with increasing contact pressure. In contrast, our analysis revealed a counter-intuitive result: samples with elevated contact pressure exhibited inferior SBS. This discrepancy is attributed to the cumulative effects of heightened contact pressure, along with other factors such as lower temperature and higher print speed. These variables could influence the flow characteristics of the PETG matrix, consequently impacting the uniformity of towpreg impregnation.

Fig. 4 also highlights the most relevant elements that compose the microstructure of the printed composites. It can be seen that they have clusters of towpregs, PETG-rich (i.e., resin-rich) areas, and voids. Most of the voids are intra-bead voids, which are specific of parts 3D printed with FFF technology. While most voids in the microstructure are circular, some ellipsoidal shapes can be seen sparingly. When examining the optical micrographs at lower magnifications, sub-perimeter voids become apparent. These voids form between turning rasters along the perimeter of the parts - a result of physical limitations during filament deposition [31]. Inter-layers and intra-layers voids are also observed. These are impossible to be avoided due to intrinsic characteristics of the printing process, in which complete filling with material and perfect material flow are extremely difficult to be controlled. In an ideal scenario where 100% coalescence occurs between two adjacent rasters, the existence of this type of void would be physically implausible [32].

Fig. 5 displays CT scans of the same samples, which provide a more profound and detailed insight into the microstructures of the specimens. The 3D rendering of the samples clearly shows that the microstructures do not have perfect structure between layers, especially sample 0.24_200_0.6, which makes the sample more prone to delamination when under shear-dominated loading. Moreover, the void fraction can be determined from these images, which is 10.0% ± 5.3% and 12.1% ± 2.6% for samples 0.24_200_0.6 and 0.34_220_0.5, respectively. These void fractions are calculated from nine sub-volumes within each sample. It can also be seen that the layer structure for the specimen 0.34_220_0.5 is more homogeneous than that of sample 0.24_200_0.6. This aligns with the observations made from the optical micrographs, as well as the accuracy of the determined void contents.

3.2. Mechanical response & failure analysis

Fig. 6 presents the load × displacement curves for all 18 families of composites. The results are presented as error band plots, where

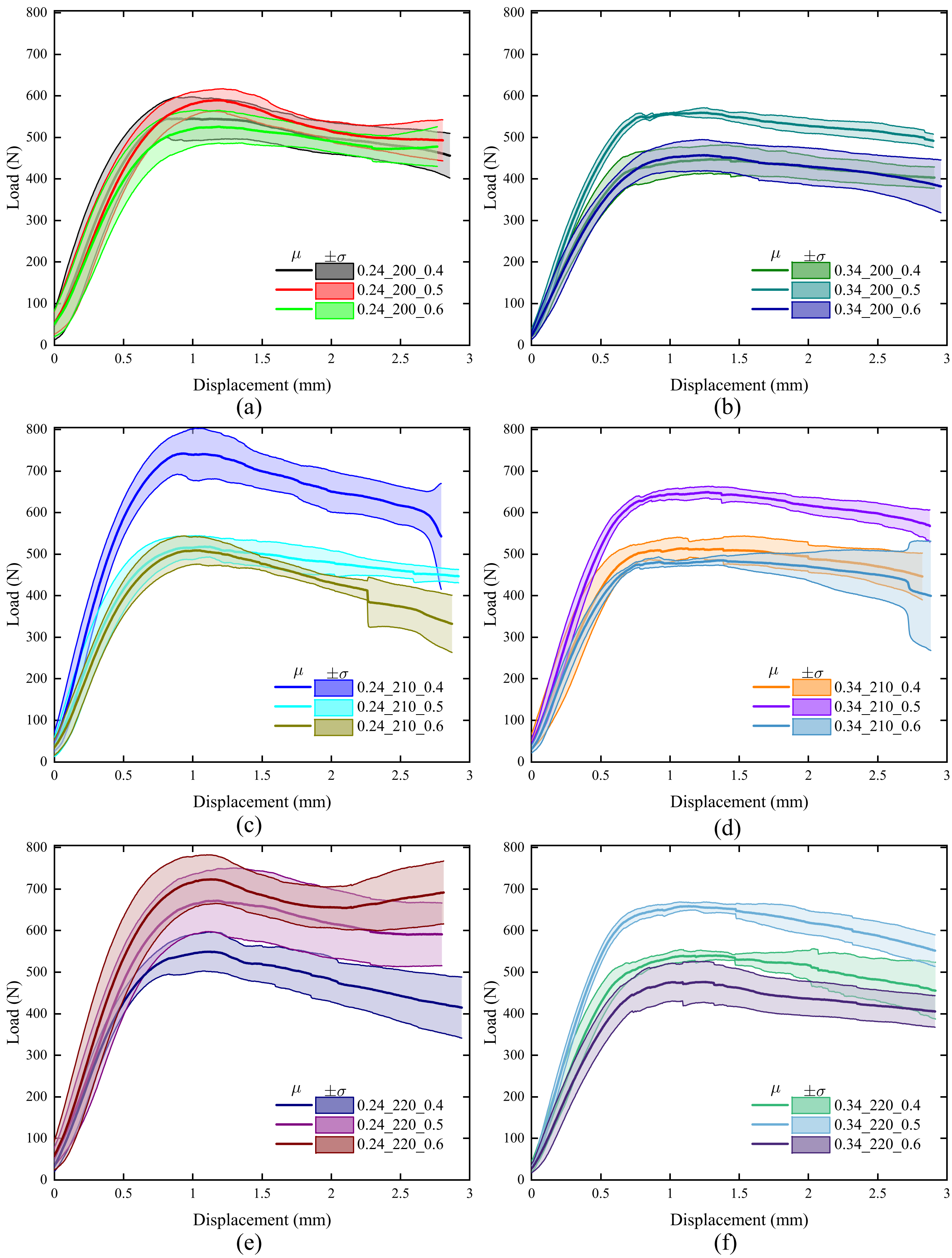

Fig. 6. Error band plots (average (μ) with one standard deviation ($\pm 1\sigma$)) for all samples, considering five samples of each family of composites.

each error band is composed of the average (μ) and one standard deviation ($\pm 1\sigma$) for 5 validated samples of every family of samples. Each plot is composed of three error band plots for better visualisation of the results. The initial non-linearity is due to the establishment of contact between the loading/support noses and the sample. All curves have the typical shape of ductile materials, which is characterised by one load peak followed by long plastic deformation. The load–displacement curves have a slight non-linearity up to the peak load,

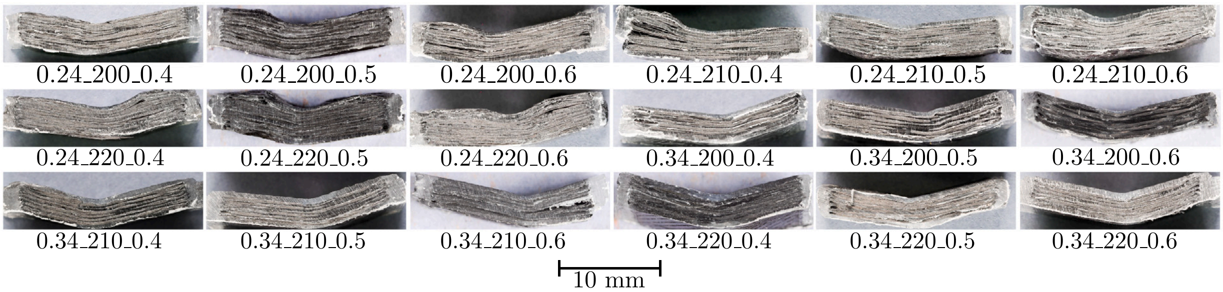

Fig. 7. Photographs of all fractured samples.

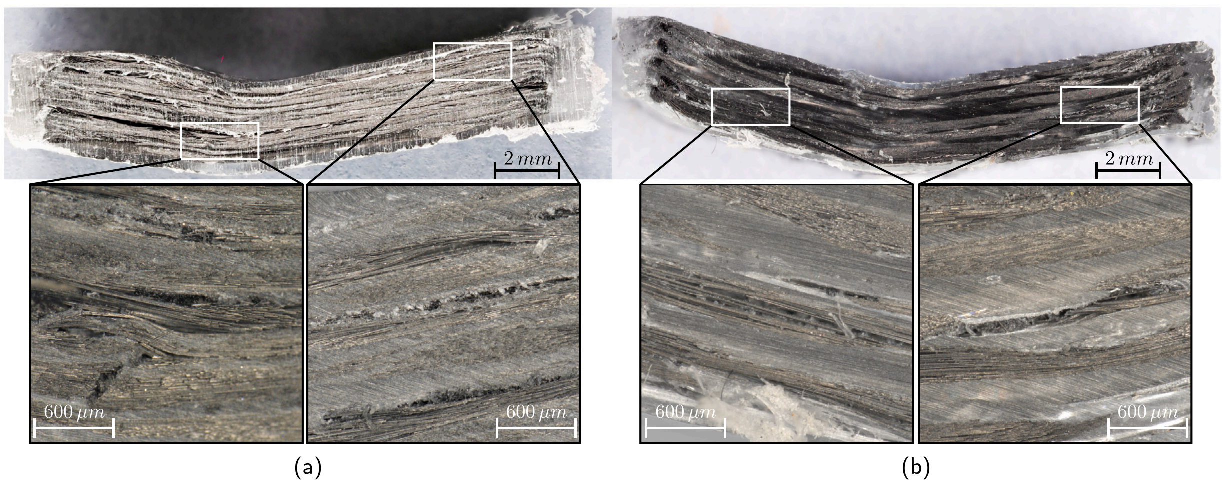

Fig. 8. Stereo micrographs highlighting fractured areas for samples (a) 0.24_200_0.6 and (b) 0.34_200_0.6.

associated with damage nucleation that arises from shear tests, which are usually non-linear. Thereafter, a nearly steady state takes place for all curves due to plastic damage propagation, which is mainly driven by the thermoplastic matrix. Another observation is the high likelihood of strong printing parameters influencing the SBS of the composites.

Typical failure modes observed in the short beam tests are shown in Fig. 7. As can be seen, only typical shear failure modes are identified, mostly dominated by horizontal minor and major cracks and large delaminations throughout the width and length of the samples. Similar failure modes are observed by Adams and Lewis [33], Silva et al. [34], and Gagabi et al. [35].

The typical failure modes are illustrated in Fig. 8, which shows magnified stereographic images of fracture samples 0.24_200_0.6 and 0.34_200_0.6. These two samples are selected because, from the microstructural point of view, samples with the same macrolayer thickness have similar microstructure, therefore, one sample of each macrolayer thickness has been selected to match the microstructure of the parts depicted in Fig. 2. In general, it is observed that in the samples with a layer thickness of 0.24 mm, the cracks are more pronounced than in samples with a layer thickness of 0.34 mm.

Fig. 9 depicts CT scans of two fractured samples: 0.24_200_0.6 and 0.34_220_0.5 (CT scans of their microstructures are shown in Fig. 5). They include both 2D scans and 3D renderings of the samples. These CT scans confirm valid fracture modes for the samples, mostly delaminations, and also provide a richer view of their microstructures. The void fractions of these samples have changed in different ways after being tested. For example, sample 0.24_200_0.6, where delaminations are clearly visible and pronounced, the void content has increased from 10.0% ± 5.3% (before testing) to 25.9% ± 7.8% after tested. The main reason for this substantial increase is the high amount of delaminated areas. On the other hand, the sample 0.34_220_0.5 present a decrease of its void fraction, going from 12.1% ± 2.6% (before testing) to 5.7% ± 3.2% (after testing). The primary explanation is that this sample exhibits multiple short horizontal cracks (along the fibre direction) rather than substantial delaminations. As a result, it presents smaller open volumes, justifying the lower void content compared to the measurement obtained before testing. It is worth mentioning that, for both samples, the void content is high around the edges and low at the middle of the samples. This is expected because the fibres are deposited in zigzag patterns along the edges.

These observations regarding the void formation align with expectations and earlier discussion about Figs. 4,5, considering that the fibres are deposited in zigzag trajectories at the edges, in which the different compaction along the edges increase the likelihood of creating voids. The contour (edges) of the printed parts are composed of the external shell and plastic perimeters, in addition to the fibre deposition following zigzag trajectories. Both external shell and plastic perimeters are filled with rasters (or beads). It can be seen in Figs. 5,9 that raster gaps are present due to the separation of neighbouring rasters, which is caused by improper infill of material in these zones. Furthermore, the contact between the composite layers and plastic perimeter, and the contact between plastic perimeter and external shell are not perfect. Consequently, the probability of gap formation rises, leading to the void fommation.

3.3. Statistical analysis

A comprehensive statistical treatment is herein carried out to better understand the trends, significance, relevance, effects, and interactions between variables. A 3-way ANOVA is then utilised to determine whether there is a 3-way relationship among the three independent variables on the dependent outcome. Three-way ANOVA is chosen here because there are three print parameters (extruder temperature, print speed, and layer height), which are considered independent variables

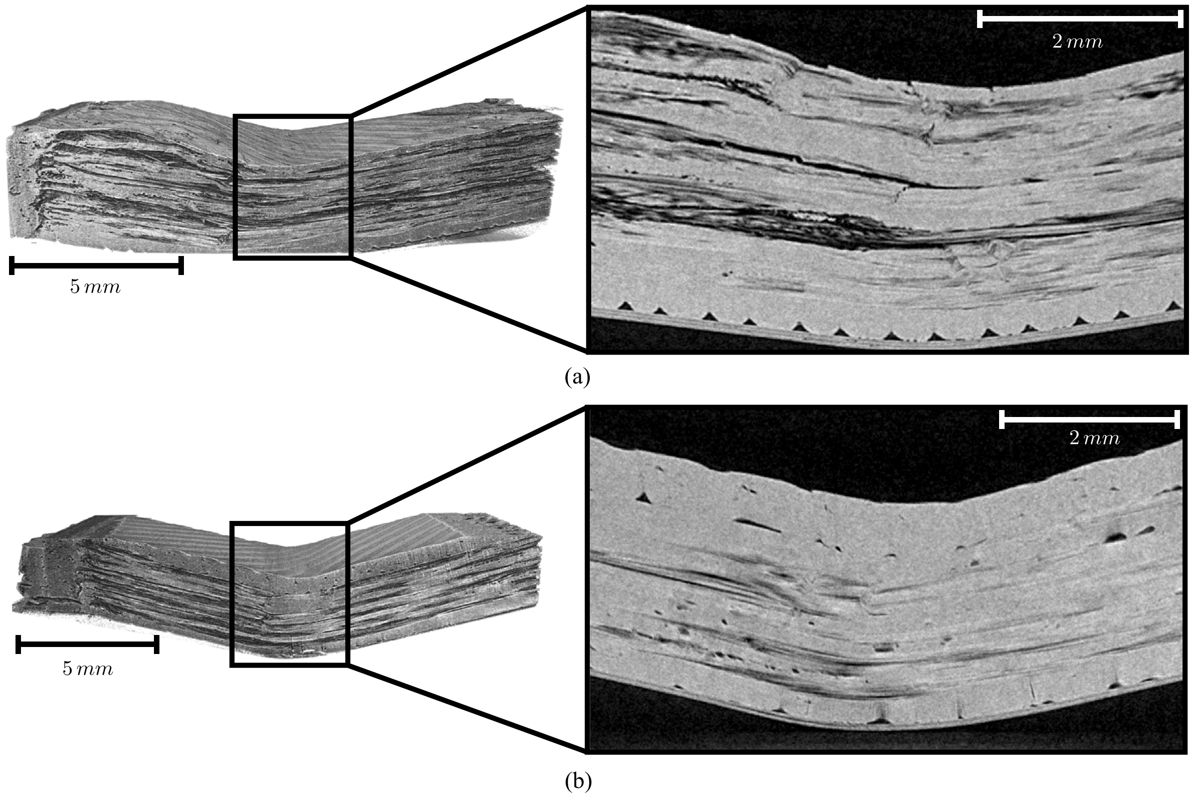

Fig. 9. CT scans of fracture samples (a) 0.24_200_0.6 and (b) 0.34_220_0.5. 3D renders are shown on the left side while 2D zoomed-in cross-sections are on the right side.

Table 3
Three-way ANOVA results on the short beam strength as a function of extruder temperature, print speed, and layer height.

Variables	DoF	SS	MS	F value	Pr(>F)	Significance
Extruder Temperature	2	196.69	98.35	121.31	<2 e−16	***
Print speed	2	70.56	35.28	43.52	4.08e−13	***
Layer height	1	58.87	58.87	72.61	1.63e−12	***
Extruder Temperature : Print speed	4	33.35	8.34	10.28	1.21e−06	***
Extruder Temperature : Layer height	2	21.62	10.81	13.34	1.18e−05	***
Print speed : Layer height	2	46.72	23.36	28.81	6.41e−10	***
Extruder Temperature : Print speed : Layer height	4	13.23	3.31	4.08	0.00489	**
Residuals	72	58.37	0.81			

DoF: degrees of freedom; SS: sum of squares; MS: mean squares; Pr(>F): p-value Significance codes: 0: '***'; 0.001: '**'; 0.01: '*'; 0.05: '.'; 0.1: '–'.

(factors), and one dependent variable - the short beam strength (SBS). This represents a complex set of data with 18 possible interactions, and then understanding and quantifying whether one or more interactions may influence the outcome becomes possible.

Initially, to explore potential trends in the raw data, a facetted grid of point plots is presented in Fig. 10. Since these results do not have any statistical treatment, they are better understood together with a box plot (Fig. 11) of the same combination of variables, that is, the SBS × extruder temperature, grouped by layer height, and facetted by the print speed.

Analysing both Figs. 10 and 11 together, it can be observed that there is considerable variation in SBS between the different sets of printing parameters. The box plot (Fig. 11) can clearly show the composites printed with different parameters have considerable variation on the SBS (i.e., 0.24_210_0.5 and 0.34_200_0.6), families with potential outliers (data points outside of their "boxes" in Fig. 11: 0.34_200_0.4, 0.34_220_0.4, 0.24_220_0.5, 0.24_210_0.6, 0.23_220_0.6), the family with the lowest mean SBS (0.24_200_0.6), and the printing set that gives the highest SBS (0.34_220_0.5). This way of presenting the results can provide a useful and quick visual summary of the variability of values in a dataset. Further statistical analyses are required to better understand the influence of every printing condition and every independent variable on the SBS. For this reason, ssveral statistical tests are herein carried out, as follows next.

Table 3 exhibits the results of a three-way ANOVA test conducted on SBS, examining its dependence on extruder temperature, print speed, and layer height. The findings indicate significance across all factors and all interactions between variables, given their probability values (Pr) lower than 1% (0.01). This threshold signifies the probability that the null hypothesis is false. A lower Pr value means that the null hypothesis can be reliably rejected, indicating statistical significance in the test. Conversely, a Pr greater than 0.01 suggests the absence of significant effects between variables, which has not been observed here.

Nonetheless, further assumptions are made to conclude effects and interactions. This is done through a visual diagnostic of the 3-way ANOVA model developed from the dataset, as depicted in Fig. 12. In general, the diagnostic plots presented in Fig. 12 are highly favourable. Specifically, Fig. 12(a) serves as a valuable tool for identifying outliers and assessing the correlation between residuals and predicted values. If a discernible trend, such as an upward/downward trend or a zigzag line, is observed in the plot, it indicates possible concerns with the model. Fig. 12(b) reveals whether the residuals exhibit a normal distribution, which is preferable, or if they deviate from such a

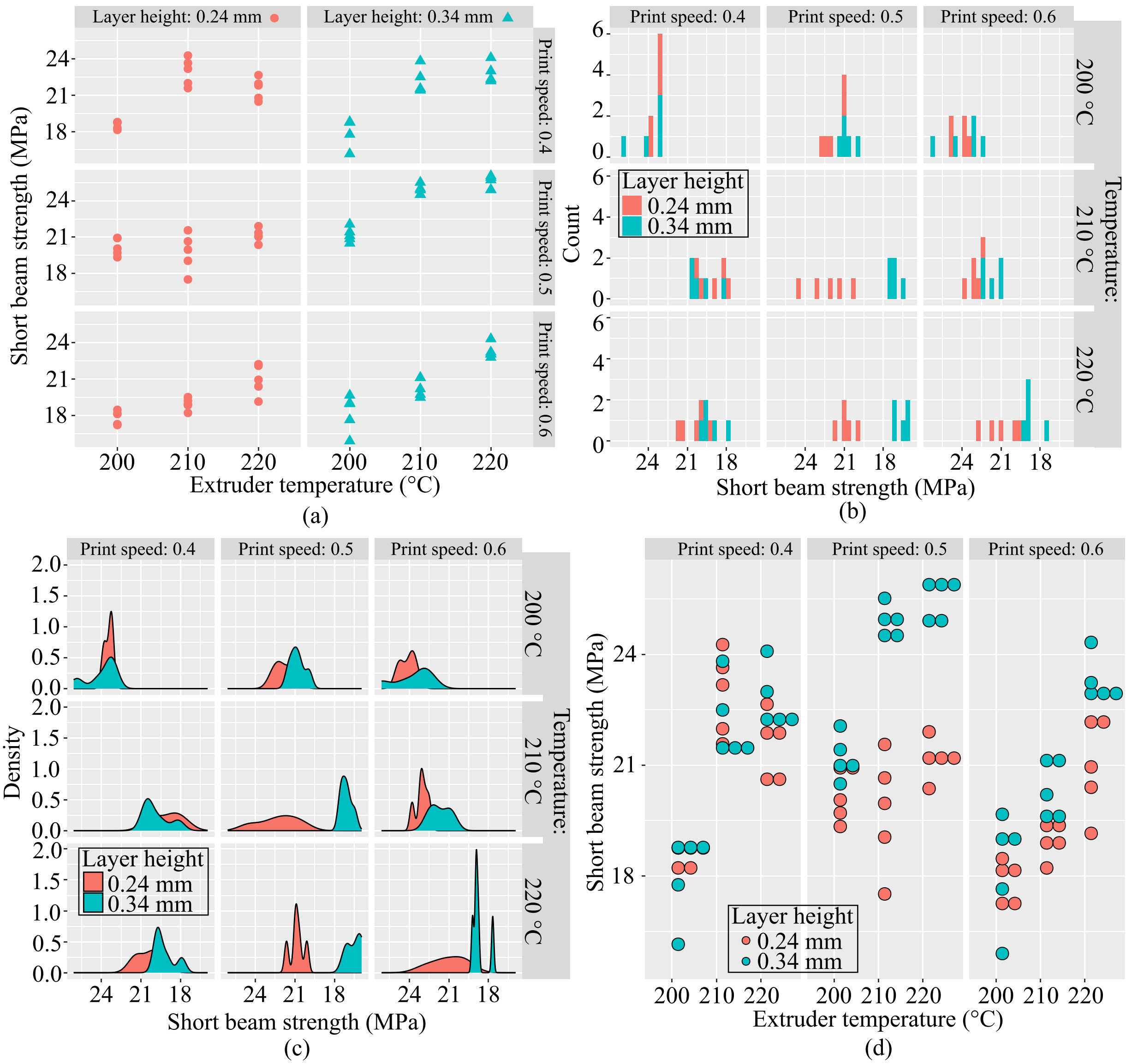

Fig. 10. Exploration of the raw data through (a) a facetted grid of point plots, (b) histograms of each factor grouped by layer height and facetted as a 2D grid of temperature:speed, (c) distributions of each factor grouped by layer height and facetted as a 2D grid of temperature: speed, and (d) dot plots of the short beam strength:extruder temperature, grouped by layer height and facetted by print speed.

distribution. If the points align to the line, it signifies that the residuals exhibit a normal distribution [36], as demonstrated in our observations (Fig. 12(b)). Fig. 12(c) offers insights into homoscedasticity, indicating whether the variance of the residuals remains consistent and does not correlate with any independent variable. In ideal situations, the plot should display a relatively flat line. The presence of a noticeable trend in the line would suggest heteroscedasticity, signifying a correlation between independent variables and residuals—this poses significant challenges for regressions [37]. Notably, in this case, a reasonably flat line is observed, confirming the homoscedasticity of the data. The plot of residuals × factors (Fig. 12(d)) displays residuals plotted against chosen factors, assessing whether the unexplained variance by the model differs across various levels of the factor [38]. In a satisfactory scenario, the plot should showcase a random scatter, which is the case observed in Fig. 12(d). Alternatively, a noticeable curvature may indicate a systematic influence of independent factors that the model has not been able to accommodate.

Next, specific quantitative tests for homoscedasticity (constant variance of the residual error across groups) and normality can be run to confirm interpretations from visual diagnostics. The equality of variances represents the variances of the different groups, which should be equal in the populations (homoscedasticity). This assumption can be tested graphically (e.g., through a box plot or dot plot), or more formally via Levene's test [39], which is employed here. Starting with homoscedasticity, Table 4 presents Levene's statistic test and the significance. In alignment with the previous discussion about homoscedasticity in Fig. 12, in Levene's test, a probability above the significance criteria (0.01) means that the data has a homogeneous variance. Thus, the model passes the test.

Table 4
Homogeneity test of variances (homoscedasticity) through Levene's test.

df1	df2	Levene's statistic	Significance (p)
17	72	0.820	0.666

Normality can be quantitatively checked with the Shapiro–Wilk test. This test is a statistical test used to check if a continuous variable follows a normal distribution. The null hypothesis (H_0) states that the variable is normally distributed, and the alternative hypothesis (H_1) states that the variable is not normally distributed. After running this

Table 5
The Shapiro–Wilk test results.

No.	Independent variables			Dependent variable	Statistic	p-value
	Layer height	Extruder temperature	Print speed	SBS		
1	0.24	200	0.4	SBS	0.798	0.078
2	0.34	200	0.4		0.763	0.039
3	0.24	200	0.5		0.888	0.349
4	0.34	200	0.5		0.982	0.944
5	0.24	200	0.6		0.856	0.214
6	0.34	200	0.6		0.893	0.372
7	0.24	210	0.4		0.942	0.683
8	0.34	210	0.4		0.799	0.079
9	0.24	210	0.5		0.983	0.949
10	0.34	210	0.5		0.900	0.412
11	0.24	210	0.6		0.963	0.832
12	0.34	210	0.6		0.866	0.249
13	0.24	220	0.4		0.939	0.658
14	0.34	220	0.4		0.807	0.093
15	0.24	220	0.5		0.974	0.902
16	0.34	220	0.5		0.829	0.137
17	0.24	220	0.6		0.928	0.586
18	0.34	220	0.6		0.793	0.072

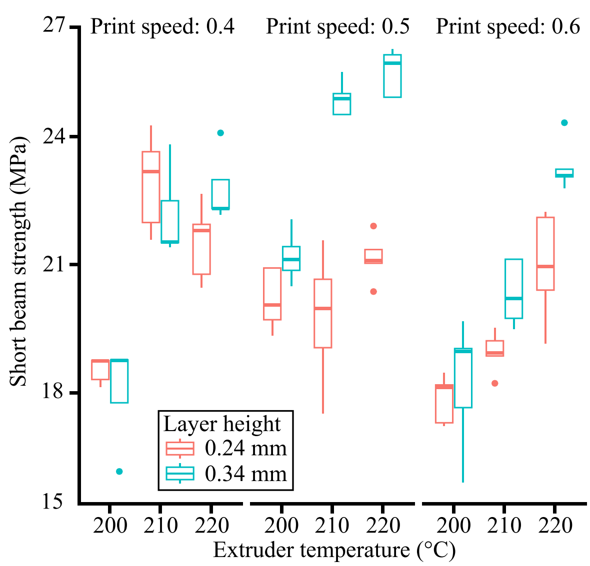

Fig. 11. Box plot of short beam strength against extruder temperature, grouped by layer height, and facetted by print speed.

test on residuals of ANOVA, the residuals reveal a $W = 0.977$ and a $p = 0.110$. A Shapiro–Wilk test with a p-value > 0.01 means that the null hypothesis cannot be rejected, which means that the test does not show evidence of non-normality (see Table 5).

As can be seen from the results, normality is not violated and the assumptions are confirmed. However, a deeper statistical treatment of the data is appropriate through a post-hoc analysis. First, a fit of the overall model, the main factors, and their interactions can be examined using a calculation of the sum of all effects, sums-of-squares relative to total sum-of-squares (analogous to R^2 for linear regression), as well as the eta squared (η^2) test for individual effect and interactions. These results are summarised in Table 6. The value of η^2 may vary between 0 and 1, with values closer to 1 indicating that a specific variable in the model can explain a greater fraction of the variation, whereas values close to 0 mean that the specific variable represents a lower fraction of the overall variation. The overall variance explained by the model is $R^2 = 0.883$, and adjusting for the number of observations and factors is $R^2_{adj} = 0.855$.

Next, the proportion of variance explained by main effects and interactions using η^2 for each case can be calculated, as shown in Table 7. This confirms that extruder temperature has the largest effect ($\eta^2 =$ 0.394), followed by print speed ($\eta^2 = 0.141$) and layer height ($\eta^2 =$ 0.118). Secondly, regarding interactions, the interaction between print speed:layer height has the greatest effect, followed by the interactions between extruder temperature:print speed, extruder temperature:layer height, and then followed by the three-way interaction of extruder temperature:print speed:layer height.

Table 6
Calculation of overall variances for further eta squared (η^2) post-hoc test for effects and interactions.

MS_r	MS_t	R^2	R^2_{adj}	SS_e	SS_r	SS_t
0.811	5.611	**0.883**	**0.855**	441.025	58.368	499.393

MS_r: mean squares residual; MS: mean squares total; R^2_{adj}: Adjusted R-squared for a no. of predictions in the model; SS_e: sum of squares of an effect; SS_r: residuals of sum of squares; SS_t: total sum of squares.

4. Conclusions

A comprehensive experimental research was conducted to investigate the impact of 3D printing parameters on the interlaminar shear strength of 3D printed composite. The layer height, extruder temperature, and print speed were varied and tested in short beam tests, totalling 18 different sets of composites. A three-way ANOVA statistical treatment was applied to the dataset, and a comprehensive series of statistical tests was applied to quantify the influence of each variable on the outcome and check whether there is significance in the impact of different printing parameters on the short beam strength. Stereo and optical microscopy, along with X-ray CT scanning, were taken to analyse both the microstructure and failure mechanisms of the printed composites.

The results revealed excellent repeatability on the load–displacement curves, which was observed in low deviations both in the linear portion of the curves within each family and low errors on the peak load. The samples printed with a layer thickness of 0.34 mm, extruder temperature of 220 °C, and print speed of 5 mm/s (print coefficient of 0.5) had the highest mean short beam strength, whereas the samples printed with a thickness of 0.24 mm, extruder temperature of 200 °C, and print speed of 6 mm/s had the lowest SBS. It is concluded and recommended to use print speed of 5 mm/s, extruder temperature of 220 °C, and a layer height of 0.34 mm to 3D print continuous carbon fibre reinforced epoxy-PETG composites with higher interlaminar strength.

The micrographs and CT scans of fractured samples showed that minor horizontal cracks and delaminations were the dominant failure modes. The samples 0.24_200_0.6 and 0.34_220_0.5 had the lowest and highest short beam strength, respectively, because of their differences

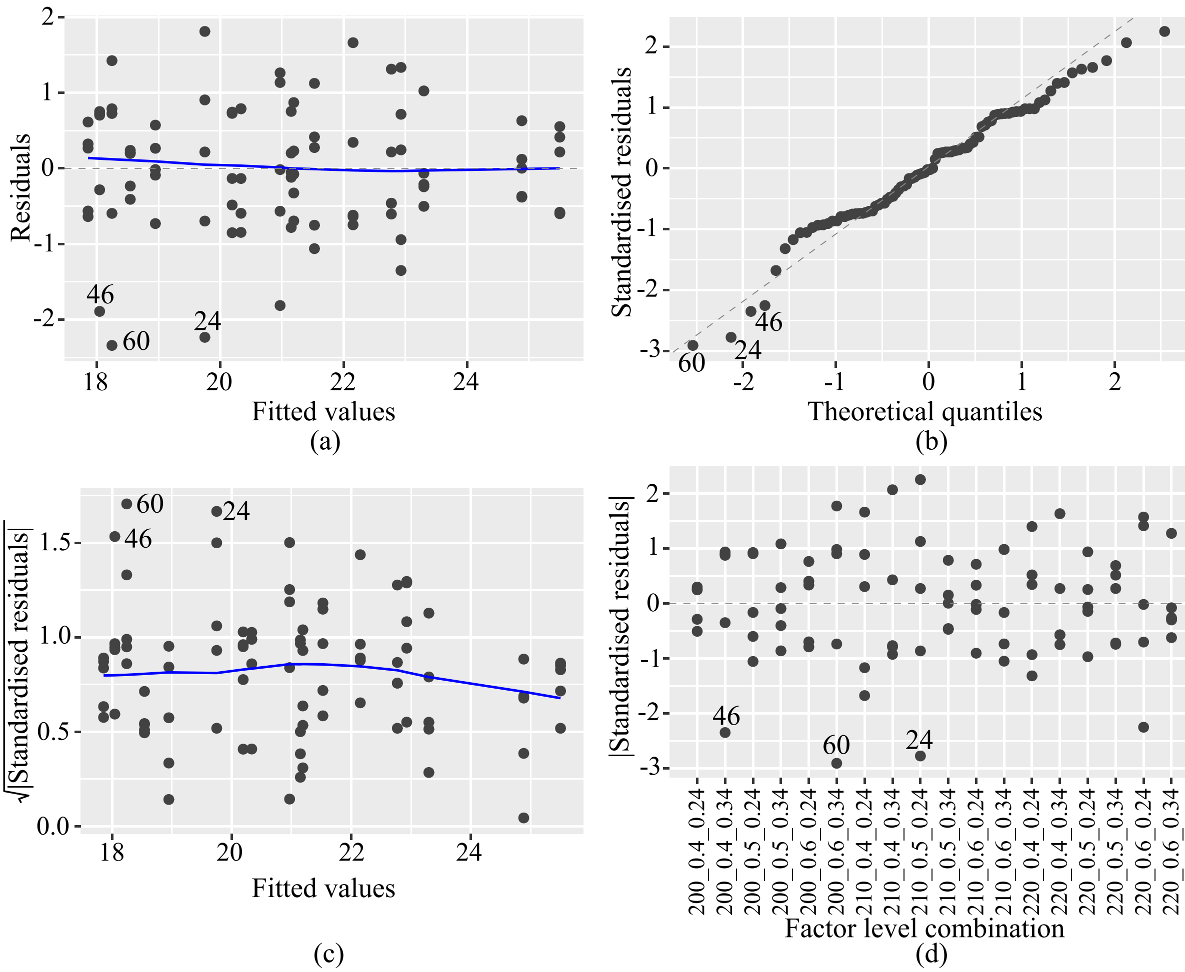

Fig. 12. Visual diagnostic plots of the statistical model by showing residuals in four different ways: (a) residuals × fitted values; (b) normal Q-Q plot to show if residuals are normally distributed; (c) scale-location plot to show if residuals are spread equally along the ranges of predictors to check the assumption of equal variance (homoscedasticity); and (d) residuals × leverage to find out if there are influential cases (combinations of parameters). The three most extreme points – outliers – are reported in every residual plot.

Table 7
Effects and interactions between variables using the η^2 test.

Extruder temperature (T)	Print speed (S)	Layer height (H)	T:S	T:H	S:H	T:S:H
0.394	0.142	0.118	0.067	0.043	0.093	0.026

in their microstructure, which is more homogeneous and compact for the specimen 0.34_220_0.5. Although these two samples showed no significant difference in void contents before testing, the void fraction for the sample 0.24_200_0.6 increased after testing, whereas the void content decreased for the sample 0.34_220_0.5 after testing. This is because of large delaminations observed for the sample 0.24_200_0.6, while specimen 0.34_220_0.5 showed short cracks, thus having less open volumes. The statistical tests confirmed that there is a significant difference among the 18 different sets of printing parameters. A posthoc analysis using the η^2 test for individual effects and interactions related that the extruder temperature is the most influential printing parameter, followed by print speed and layer height.

CRediT authorship contribution statement

José Humberto S. Almeida Jr.: Conceptualization, Data curation, Formal analysis, Investigation, Methodology, Software, Validation, Visualization, Writing – original draft. **Siddharth Jayaprakash:** Conceptualization, Investigation, Methodology, Validation, Writing – original draft. **Kari Kolari:** Conceptualization, Funding acquisition, Investigation, Methodology, Validation. **Jukka Kuva:** Investigation, Methodology, Visualization. **Kirsi Kukko:** Investigation, Visualization. **Jouni Partanen:** Funding acquisition, Project administration, Supervision.

Declaration of competing interest

The authors declare that they have no known competing financial interests or personal relationships that could have appeared to influence the work reported in this paper.

Data availability

All required data for replicating the results can be found in the Supplementary Material and Appendix of this article. In addition, the raw images from the CT scans can be found here: DOI: https://doi.org/10.23729/ebe7a8e4-1a16-4dac-8867-015b07cd3971.

Acknowledgements

HA is supported by the Royal Academy of Engineering under the Research Fellowship scheme [Grant no. RF/201920/19/150]. SJ, KK, KK, and JP thank Strategic Research Council and Academy of Finland as part of the ValueBioMat project [Grant nos. 327248 and 352429]. We acknowledge Hanna Iitti (from VTT) for her assistance with the micrographs. HA expresses gratitude to Dr Alex Lennon (from QUB) for the insightful discussion regarding the statistical analysis techniques. X-ray tomography was supported by Academy of Finland via the RAMI infrastructure [Grant no. 293109].

Appendix A. Implementation of the statistical analysis

The statistical analysis presented in this work has been developed using the following chunks of codes. They are written in R language and need to be run in RStudio environment.

Chunk 1: Importing data

````
```{r include=FALSE}
# clean environment
rm(list = ls()) # remove objects from session
gc() # rubbish collection - free up memory

# set some default code chunk behaviour
knitr::opts_chunk$set(message=FALSE, warning=FALSE, error=FALSE)

# load and install any required packages
# "pacman" is used to install any later requested packages for the session
# if (!require("pacman")) install.packages("pacman")
# load requried packages for the session
pacman::p_load(tidyverse,readxl,rstatix,ggfortify,ggprism)
```
````

Chunk 2: Data transformation

````
```{r}
# set working directory, file name, read data
workingPath = dirname(rstudioapi::getActiveDocumentContext()$path)
setwd(workingPath)
fname = stringr::str_c(workingPath,"/your_file.xlsx")
raw.df = readxl::read_xlsx(fname, sheet = "your_data", skip = 1)

# display HTML table of original input variables
raw.df %>%
    select(`Layer height`,
           `Extruder temp.`,
           `Print Speed coefficient`, `SBS`)
# Create a new data frame to ease handling with other commands later
# and to avoid overwriting the raw data
# Also, ensure explanatory variables are treated as "factors" to ensure
# correct interpretation by ANOVA functions
tmp.df = tibble(SBS = as.numeric(raw.df$`SBS`))
tmp.df$LayerHeight = as.factor(raw.df$`Layer height`)
tmp.df$ExtruderTemp = as.factor(raw.df$`Extruder temp.`)
tmp.df$PrintSpeed = as.factor(raw.df$`Print Speed coefficient`)
```
````

Chunk 3: Data exploration

````
```{r}
# pipe data frame into a ggplot frame or response vs extruder temp.
# specify point (geometries) as plot type, and facet by print speed and layer height
tmp.df %>%
  ggplot(aes(x = ExtruderTemp, y = SBS, colour = LayerHeight, group=LayerHeight, shape=LayerHeight)) +
    geom_point(size=3) +
    facet_grid(PrintSpeed~LayerHeight, labeller = label_both)
```
# Box plot of SBS vs extruder temp., grouped by layer height facetted by print speed
tmp.df %>%
  ggplot(aes(x=ExtruderTemp,y=SBS, colour=LayerHeight)) +
  geom_boxplot() +
  facet_grid(~PrintSpeed, labeller = label_both) +
  theme_prism() + theme(legend.title = element_text())
```
````

Chunk 4: Analysis

````
```{r}
# Compute and summarise a 3-way ANOVA on SBS as a function of
# extruder temp., print speed, and layer height
anova.3way = aov(SBS ~ ExtruderTemp*PrintSpeed*LayerHeight, data = tmp.df)
summary(anova.3way)
```
````

Chunk 5: Diagnostics

````
```{r}
# diagnostics
autoplot(anova.3way)
```
```{r}
# homoscedasticty (constant variance)
# Levene test syntax is similar to format used for `aov` function
rstatix::levene_test(tmp.df, SBS ~ LayerHeight*ExtruderTemp*PrintSpeed)
```
```{r}
# Shapiro-Wilk on residuals of ANOVA model using standard version
shapiro.test(x = residuals(anova.3way))
```
```{r}
# Shapiro-Wilk on all group combinations using rstatix version
tmp.df %>%
   group_by(ExtruderTemp, PrintSpeed, LayerHeight) %>%
   rstatix::shapiro_test(SBS)
```
````
````

Chunk 6: Post-hoc analysis

```
```{r}
# Calculate overall variance explained first
SS_resid = sum((fitted(anova.3way)-tmp.df$SBS)
    ^2)
SS_explain = sum((fitted(anova.3way) - mean(tmp.
    df$SBS))^2)
SS_total = SS_resid + SS_explain
Rsq = SS_explain/SS_total
Rsq # display it in output
MS_resid = SS_resid/72
MS_total = SS_total/89
Rsq_adj = 1 - MS_resid/MS_total
Rsq_adj # display it in output
```
```{r}
# These can be calculated using the rstatix
    package
effectFits = rstatix::eta_squared(anova.3way)
effectFits
```
```{r}
# perform Tukey's HSD test on all contrasts from
     the ANOVA model
TukeyHSD(anova.3way)
```
```{r warning=FALSE}
# histograms of each factor, grouped by layer
    height and facetted as
# 2D grid of temp. vs speed
tmp.df %>%
  ggplot(aes(x=SBS, fill=LayerHeight)) +
  geom_histogram() +
  facet_grid(ExtruderTemp~PrintSpeed, labeller =
     label_both)
# distributions of each factor, grouped by layer
     height and facetted as
# 2D grid of temp. vs speed
tmp.df %>%
  ggplot(aes(x=SBS,fill=LayerHeight)) +
  geom_density() +
  facet_grid(ExtruderTemp~PrintSpeed, labeller =
     label_both)
# dot plots of SBS vs extruder temp., grouped by
     layer height, and facetted by speed
tmp.df %>%
  ggplot(aes(x=ExtruderTemp,y=SBS, fill=
    LayerHeight)) +
  geom_dotplot(binaxis = 'y') +
  facet_wrap(~PrintSpeed)
```
```

Appendix B. Supplementary data

Supplementary material related to this article can be found online at https://doi.org/10.1016/j.compstruct.2024.118034.

References

[1] Monticeli FM, Neves RM, Ornaghi Junior HL, Almeida Junior JHS. Prediction of bending properties for 3D-printed carbon fibre/epoxy composites with several processing parameters using ANN and statistical methods. Polymers 2022;14(17). http://dx.doi.org/10.3390/polym14173668.

[2] Liu F, Ferraris E, Ivens J. Mechanical investigation and microstructure performance of a two-matrix continuous carbon fibre composite fabricated by 3D printing. J Manuf Process 2022;79:383–93. http://dx.doi.org/10.1016/j.jmapro.2022.04.050.

[3] Bragaglia M, Cecchini F, Paleari L, Ferrara M, Rinaldi M, Nanni F. Modeling the fracture behavior of 3D-printed PLA as a laminate composite: Influence of printing parameters on failure and mechanical properties. Compos Struct 2023;322:117379. http://dx.doi.org/10.1016/j.compstruct.2023.117379.

[4] Wang X, Jiang M, Zhou Z, Gou J, Hui D. 3D printing of polymer matrix composites: A review and prospective. Composites B 2017;110:442–58. http://dx.doi.org/10.1016/j.compositesb.2016.11.034.

[5] Christoff BG, Almeida, Jr. JHS, Cardoso EL, Tita V. A multiscale topology optimisation framework for hollow spheres as cellular materials. Eng Struct 2023;284:115990. http://dx.doi.org/10.1016/j.engstruct.2023.115990.

[6] Almeida, Jr. JHS, Christoff BG, Tita V, St-Pierre L. A concurrent fibre orientation and topology optimisation framework for 3D-printed fibre-reinforced composites. Compos Sci Technol 2023;232:109872. http://dx.doi.org/10.1016/j.compscitech.2022.109872.

[7] Srivastava C, Agostino P, Stamopoulos AG, Alcock B, Strandlie A, Grammatikos S. Three-dimensional analysis of porosity in as-manufactured glass fiber/vinyl ester filament winded composites using X-ray micro-computed tomography. Appl Compos Mater 2023. http://dx.doi.org/10.1007/s10443-023-10167-z.

[8] Hou Z, Tian X, Zhang J, Zheng Z, Zhe L, Li D, et al. Optimization design and 3D printing of curvilinear fiber reinforced variable stiffness composites. Compos Sci Technol 2021;201:108502. http://dx.doi.org/10.1016/j.compscitech.2020.108502.

[9] Zhang H, Wang S, Zhang K, Wu J, Li A, Liu J, et al. 3D printing of continuous carbon fibre reinforced polymer composites with optimised structural topology and fibre orientation. Compos Struct 2023;313:116914. http://dx.doi.org/10.1016/j.compstruct.2023.116914.

[10] Maqsood N, Rimašauskas M. Development and fabrication of continuous carbon fiber reinforced thermoplastic porous composite structures with different infill patterns by using additive manufacturing. J Thermoplast Compos Mater 2023;36(5):2050–75. http://dx.doi.org/10.1177/08927057221088468.

[11] Tian X, Liu T, Yang C, Wang Q, Li D. Interface and performance of 3D printed continuous carbon fiber reinforced PLA composites. Composites A 2016;88:198–205. http://dx.doi.org/10.1016/j.compositesa.2016.05.032.

[12] Penumakala PK, Santo J, Thomas A. A critical review on the fused deposition modeling of thermoplastic polymer composites. Composites B 2020;201:108336. http://dx.doi.org/10.1016/j.compositesb.2020.108336.

[13] Kabir SMF, Mathur K, Seyam A-FM. A critical review on 3D printed continuous fiber-reinforced composites: History, mechanism, materials and properties. Compos Struct 2020;232:111476. http://dx.doi.org/10.1016/j.compstruct.2019.111476.

[14] Safari F, Kami A, Abedini V. 3D printing of continuous fiber reinforced composites: A review of the processing, pre- and post-processing effects on mechanical properties. Polym Polym Compos 2022;30:09673911221098734. http://dx.doi.org/10.1177/09673911221098734.

[15] Zhang Z, Xu J, Ma Y, Sun M, Chai H, Wu H, et al. Design and analysis of multistable curvilinear-fiber laminates based on continuous fiber 3D printing of thermosetting resin matrix. Compos Struct 2023;307:116616. http://dx.doi.org/10.1016/j.compstruct.2022.116616.

[16] Ding S, Zou B, Zhuang Y, Wang X, Feng Z, Liu Q. Effect of printing design and forming thermal environment on pseudo-ductile behavior of continuous carbon/glass fibers reinforced nylon composites. Compos Struct 2023;322:117362. http://dx.doi.org/10.1016/j.compstruct.2023.117362.

[17] Dou H, Cheng Y, Ye W, Zhang D, Li J, Miao Z, et al. Effect of process parameters on tensile mechanical properties of 3D printing continuous carbon fiber-reinforced PLA composites. Materials 2020;13(17). http://dx.doi.org/10.3390/ma13173850.

[18] Rimašauskas M, Jasiūnienė E, Kuncius T, Rimašauskienė R, Cicėnas V. Investigation of influence of printing parameters on the quality of 3D printed composite structures. Compos Struct 2022;281:115061. http://dx.doi.org/10.1016/j.compstruct.2021.115061.

[19] Dong K, Ke H, Panahi-Sarmad M, Yang T, Huang X, Xiao X. Mechanical properties and shape memory effect of 4D printed cellular structure composite with a novel continuous fiber-reinforced printing path. Mater Des 2021;198:109303. http://dx.doi.org/10.1016/j.matdes.2020.109303.

[20] Maqsood N, Rimašauskas M. Influence of printing process parameters and controlled cooling effect on the quality and mechanical properties of additively manufactured CCFRPC. Compos Commun 2022;35:101338. http://dx.doi.org/10.1016/j.coco.2022.101338.

[21] Jia Z, Wang Q, Liu J. An investigation of printing parameters of independent extrusion type 3D print continuous carbon fiber-reinforced PLA. Appl Sci 2023;13(7). http://dx.doi.org/10.3390/app13074222.

[22] Caminero M, Chacón J, García-Moreno I, Reverte J. Interlaminar bonding performance of 3D printed continuous fibre reinforced thermoplastic composites using fused deposition modelling. Polym Test 2018;68:415–23. http://dx.doi.org/10.1016/j.polymertesting.2018.04.038.

[23] Fonseca J, Ferreira I, De Moura M, Machado M, Alves J. Study of the interlaminar fracture under mode I loading on FFF printed parts. Compos Struct 2019;214:316–24. http://dx.doi.org/10.1016/j.compstruct.2019.02.005.

[24] Azarov AV, Antonov FK, Golubev MV, Khaziev AR, Ushanov SA. Composite 3D printing for the small size unmanned aerial vehicle structure. Composites B 2019;169:157–63. http://dx.doi.org/10.1016/j.compositesb.2019.03.073.

[25] Fisher T, Almeida, Jr. JHS, Falzon BG, Kazancı Z. Tension and compression properties of 3D-printed composites: print orientation and strain rate effects. Polymers 2023;15(7). http://dx.doi.org/10.3390/polym15071708.

[26] Rasch D, Verdooren R. Determination of minimum and maximum experimental size in one-, two-and three-way ANOVA with fixed and mixed models by R. J Stat Theory Pract 2020;14(57):1–25.

[27] Derrick B, Ruck A, Toher D, White P, et al. Tests for equality of variances between two samples which contain both paired observations and independent observations. J Appl Quant Methods 2018;13(2):36–47, URL https://uwe-repository.worktribe.com/output/865549.

[28] González-Estrada E, Cosmes W. Shapiro-wilk test for skew normal distributions based on data transformations. J Stat Comput Simul 2019;89(17):3258–72. http://dx.doi.org/10.1080/00949655.2019.1658763.

[29] Richardson JT. Eta squared and partial eta squared as measures of effect size in educational research. Educ Res Rev 2011;6(2):135–47. http://dx.doi.org/10.1016/j.edurev.2010.12.001.

[30] Wang F, Wang G, Ning F, Zhang Z. Fiber–matrix impregnation behavior during additive manufacturing of continuous carbon fiber reinforced polylactic acid composites. Addit Manuf 2021;37:101661. http://dx.doi.org/10.1016/j.addma.2020.101661.

[31] Parandoush P, Lin D. A review on additive manufacturing of polymer-fiber composites. Compos Struct 2017;182:36–53. http://dx.doi.org/10.1016/j.compstruct.2017.08.088.

[32] Tao Y, Kong F, Li Z, Zhang J, Zhao X, Yin Q, et al. A review on voids of 3D printed parts by fused filament fabrication. J Mater Res Technol 2021;15:4860–79. http://dx.doi.org/10.1016/j.jmrt.2021.10.108.

[33] Adams DF, Lewis EQ. Experimental study of three- and four.point shear test specimens. J Compos Technol Res 1995;17(4):341–9. http://dx.doi.org/10.1520/CTR10454J.

[34] da Silva LV, Almeida Jr JHS, Angrizani CC, Amico SC. Short beam strength of curaua, sisal, glass and hybrid composites. J Reinf Plast Compos 2013;32(3):197–206. http://dx.doi.org/10.1177/0731684412467561.

[35] Gagani AI, Krauklis AE, Sæter E, Vedvik NP, Echtermeyer AT. A novel method for testing and determining ILSS for marine and offshore composites. Compos Struct 2019;220:431–40. http://dx.doi.org/10.1016/j.compstruct.2019.04.040.

[36] Vining G. Technical advice: Quantile plots to check assumptions. Qual Eng 2010;22(4):364–7. http://dx.doi.org/10.1080/08982112.2010.502868.

[37] Field A, Miles J, Field Z. Discovering statistics using R. SAGE; 2017.

[38] Vining G. Technical advice: residual plots to check assumptions. Qual Eng 2010;23(1):105–10. http://dx.doi.org/10.1080/08982112.2011.535696.

[39] Gastwirth JL, Gel YR, Miao W. The impact of Levene's test of equality of variances on statistical theory and practice. Statist Sci 2009;24(3):343–60. http://dx.doi.org/10.1214/09-STS301.